Emergence of a Bilaterally Symmetric Pattern from Chiral Components in the Planarian Epidermis

Cyril Basquin, Dmitry Ershov, Noémie Gaudin, Hanh Thi-Kim Vu, Bruno Louis, Jean-François Papon, Anne-Marie Orfila, Sarah Mansour, Jochen Christian Rink, Juliette Azimzadeh

Version of Record: https://www.sciencedirect.com/science/article/pii/S1534580719308688
Manuscript_1766b4ea73c966ea280182d415d924b0

Emergence of a bilaterally symmetric pattern from chiral components in the planarian epidermis

Cyril Basquin[1], Dmitry Ershov[2], Noémie Gaudin[1], Hanh Thi-Kim Vu[3], Bruno Louis[4,5,6], Jean-François Papon[4,5,7,8], Anne-Marie Orfila[1], Sarah Mansour[3], Jochen Christian Rink[3] and Juliette Azimzadeh[1,9]

[1] Université de Paris, Institut Jacques Monod, CNRS UMR7592, 75013 Paris, France.

[2] Institut Pasteur, 75015, Paris, France.

[3] Max Planck Institute for Molecular Cell Biology and Genetics, 01307 Dresden, Germany.

[4] INSERM U955, 94010 Créteil, France.

[5] CNRS ERL7240, 94010 Créteil, France.

[6] Faculté de Médecine, Université Paris-Est, 94010 Créteil, France.

[7] Hôpital Kremlin-Bicêtre, AP-HP, 94275 Le Kremlin-Bicêtre, France

[8] Faculté de Médecine, Université Paris-Saclay, 94070 Le Kremlin-Bicêtre, France.

[9] Lead contact.

Correspondence: juliette.azimzadeh@ijm.fr

Summary

Most animals exhibit mirror-symmetric body plans, yet the molecular constituents from which they are formed are often chiral. In planarian flatworms, centrioles are arranged in a bilaterally symmetric pattern across the ventral epidermis. Here, we found that this pattern is generated by a network of centrioles with prominent left-right asymmetric properties. We identify centriole components required for establishing left-right asymmetric connections between centrioles and balancing their effects to align centrioles along polarity fields. SMED-ODF2, SMED-VFL1 and SMED-VFL3 affect the assembly of centriole appendages that tether cytoskeletal connectors to position the centrioles. We further show that the medio-lateral polarization of centrioles relies on mechanisms that are partly distinct on the left and right sides of the planarian body. Our findings shed light on how bilaterally symmetrical patterns can emerge from chiral cellular organizations.

Introduction

Animals with outwardly mirror symmetric bodies, the so-called bilaterians, constitute the largest group of animals on earth. However, many of the molecular components that make up the mirror-symmetric bilaterians are intrinsically chiral, *i.e.*, exhibit broken reflection symmetry. This raises a conceptual conundrum, as Euclidean geometry precludes the construction of a mirror-symmetric structure out of chiral components without the simultaneous use of their mirrored partners. One prominent example of a chiral cellular constituent is the centriole, the evolutionarily ancient nucleating center of the microtubule cytoskeleton (Azimzadeh, 2014). Centrioles consist of nine microtubule triplets arranged in a circular arrangement. Their chirality results from the polar structure of the triplets and their placement at an angle with respect to their neighboring triplets. In many protozoa, this inherent chiral property is amplified by asymmetries between the different centriole triplets, which anchor distinct elements of the cytoskeleton and ultimately propagate the centriole chirality to chirality over the entire cell (Boyd et al., 2011; Marshall, 2012; Yubuki and Leander, 2013). The establishment of left-right asymmetry in vertebrates via the (chiral) clockwise rotation of cilia at the surface of the embryonic node – together with anterior-posterior asymmetric positioning of the nodal cilia, provides a further example of organismal asymmetry that ultimately has its roots in centriole chirality (Chen and Zhong, 2015; Hashimoto et al., 2010; Omori et al., 2017; Shinohara and Hamada, 2017). In this process, the centriole functions as the "F molecule" originally theorized by Brown and Wolpert, which specifies the orientation of the left-right axis by aligning along the two other embryonic axes (Brown and Wolpert, 1990).

However, not all centriole-nucleated structures display obvious chirality. For example, the cilia of multiciliated cells beat in a whip-like pattern and the polarization of all cilia along the polarity axes of the body plan thus allows directional mucus transport or whole animal translocation. In this case, centrioles carry two types of appendages that align with the axis of ciliary beat: the basal foot

and the ciliary rootlet. These appendages in turn anchor cytoskeletal arrays that connect centrioles to each other and to the cellular junctions (Antoniades et al., 2014; Kunimoto et al., 2012; Vladar et al., 2012; Werner et al., 2011). Polarity proteins localized at the junctions and at the centrioles regulate cytoskeleton architecture to coordinate centriole rotational polarity with the planar polarity of the epithelium (Guirao et al., 2010; Park et al., 2008; Vladar et al., 2012). Recent work from our laboratories demonstrates the long-range polarization of ciliary rootlets in the planarian ventral epidermis along the head-tail axis that is mediated by the evolutionary conserved Wnt/Planar Cell Polarity (Wnt/PCP) pathway, superimposed in the head region with a mirror-symmetric polarization component towards the body edge mediated by the Fat/Dachsous (Ft/Ds) pathway (Vu et al., 2018). Thus, in planarians and multiciliated epithelia in general, centrioles behave as bilaterally symmetric objects that align with the cardinal body axes of the bilaterian body plan.

Here, we demonstrate cryptic chirality underneath the apparent mirror-symmetry of planarian centriole alignment, which in wild-type animals is compensated by the opposing effects of the centriole components ODF2 and VFL1/VFL3. Our results provide insights into how animals can build bilaterally symmetric tissue patterns from chiral cellular constituents.

Results

Centriole components affecting planarian locomotion in a left-right asymmetric manner

Previous results have established that paralysis, loss or gross miss-alignments of planarian cilia all disrupt the smooth gliding motility of the animals and result in a secondary translocation mode via cycles of muscular contractions/elongations (previously termed "inchworming")(Azimzadeh et al., 2012; Reddien et al., 2005; Rink et al., 2009; Vu et al., 2018; Vu et al., 2015). Interestingly, we noticed that the RNAi mediated knock-down of some centriole components resulted in a qualitatively different locomotion phenotype (Azimzadeh et al., 2012; Reddien et al., 2005). Whereas in wild type animals, the translocation vector (movement direction) was always in alignment with the head-tail vector (A/P axis), RNAi animals displayed a striking miss-alignment between the two vectors (Figure 1A; Figure S1; Movie S1). Specifically, *vfl1-* and *vfl3(RNAi)* animals always translocated at an angle of - 29 ± 8 ° and - 27 ± 7 ° (counterclockwise) relative to the A/P axis, respectively, which resulted in a drift to the left. In contrast, *odf2(RNAi)* animals translocated at an angle of 28 ± 8 ° (clockwise) and drifted to the right (Figure 1B). RNAi animals exhibited a drastic reduction in locomotion speed compared to controls, particularly in *vfl1(RNAi)* animals, but nevertheless retained gliding motility (Figure 1C; Movie S1). In agreement with this, cilia were present across the ventral epidermis of RNAi animals like in control planarians (Figure 1E). High-speed imaging of cilia in live *odf2(RNAi)* and *vfl1(RNAi)* animals confirmed that cilia were motile and that beating frequency was overall comparable to control values, with only a modest decrease in *odf2(RNAi)* animals (Figure 1D; Movie S2). Cilia nevertheless appeared to beat less synchronously in RNAi animals, which likely contributed to the decrease in locomotion speed that we observed (Movie S2).

Thus, depleting the centriole components ODF2 and VFL1/3 induced left-right asymmetric locomotion phenotypes of opposite handedness. Furthermore, the persistence of gliding motility indicated maintained functionality and long-range alignment of epidermal cilia.

Sidewinder phenotypes are caused by defects in centriole rotational polarity

To determine whether the observed locomotion defects were induced by anomalies in centriole positioning, we analyzed centriole rotational polarity in RNAi-treated animals. Using an antibody against ROOTLETIN1, a component of the ciliary rootlet (Vu et al., 2018), we measured the angle vector between individual rootlets and the A/P axis (Figure 2A, B; Figure S2). Depletion of all three genes decreased the homogeneity of rootlet polarity (*i.e.* increased the circular standard deviation or CSD) in all parts of the ventral epidermis, supporting that the entire tissue was affected (Figure 2C). Overall, the mean CSD (mean of CSD values determined for each subdivision of the epidermis) increased from 19 ° in control to 41 ° in *odf2(RNAi)*, 42 ° in *vfl3(RNAi)* and up to 58 ° in *vfl1(RNAi)* animals. Decreased rootlet alignment likely contributed to the lower locomotion speed observed in RNAi animals, as coordination of ciliary beat orientation is critical for multiciliated cell function (Kunimoto et al., 2012; Park et al., 2008). In agreement, higher dispersion of rootlet angles in *vfl1(RNAi)* correlated with a stronger reduction in locomotion speed (Figure 1C). Despite increased angle dispersion, we observed highly consistent patterns of orientation in RNAi animals (Figure 2A, B, Figure S3). Rootlets were pivoted counterclockwise in *vfl1(RNAi)* and *vfl3(RNAi)* and clockwise in *odf2(RNAi)* compared to control flatworms, confirming that centriole polarity is affected. Control animals display a bilaterally symmetric rootlet pattern characterized by a gradual increase in rootlet angles along the A/P and M/L axes (splay) (Vu et al., 2018) (Figure 2A, B, D). Variation in rootlet angles along polarity axes still occurred in sidewinder animals despite the overall rotation of rootlet angles, which resulted in strikingly left-right asymmetric rootlet patterns across the ventral epidermis (Figure 2A, B, D). To determine whether these complex patterns could explain the lateral translocation that characterizes the sidewinder phenotypes, we turned to computational modelling. We developed a model based on the assumption that the net flow generated by beating cilia is locally aligned with the mean rootlet angle (Figure S4). Simulations recapitulated experimental trajectories, supporting that the observed defects in centriole rotational polarity are sufficient to

cause the sidewinder phenotypes (Figure 3A). Interestingly, the model predicted that at longer time scales, all sidewinder animals would follow a clockwise circular trajectory, which we verified experimentally (Figure 3B, C; Movies S3). Together, our data support that the sidewinder phenotypes are caused by the rotation of centrioles in the plane of the epidermis, either clockwise or counterclockwise. Thus, the sidewinder phenotypes are chirality phenotypes that uncover cryptic left/right asymmetries in centriole orientation underneath the bilateral symmetry of the wild type pattern.

Planarian ODF2 and VFL1/3 control the assembly of centriole appendages

To gain further insights into the origin of these asymmetries, we characterized the function of planarian ODF2 and VFL1/3 proteins. SMED-ODF2 is the planarian ortholog of mouse ODF2/Cenexin, a component of the basal foot (Kunimoto et al., 2012). SMED-VFL1 and SMED-VFL3 are the orthologs of centriole proteins originally identified in unicellular models (Hoops et al., 1984; Silflow et al., 2001). We obtained antibodies against planarian VFL1 and ODF2 proteins, and found that both stain centrioles across the ventral epidermis, confirming that they are centriole components in planarians (Figure 4A, B; Figure S5). We next analyzed the ultrastructure of centrioles in control and RNAi animals. In control samples, most centrioles exhibited a basal foot and a rootlet, although in a proportion of centrioles the basal foot (33 ± 7 %) or the rootlet (22 ± 1 %) were not included in the same electron microscopic section. In *odf2(RNAi)* animals, centrioles were systematically missing a basal foot, confirming data from mouse (Kunimoto et al., 2012), but rootlet assembly was unaffected (Figure 4C, D). In *vfl1(RNAi)* and *vfl3(RNAi)*, the assembly of both the basal foot and the rootlet were abnormal. In sections from *vfl1(RNAi)* animals, 80 ± 3 % centrioles had no visible basal foot and 72 ± 6 % no visible rootlet. Assuming that a similar fraction of basal feet and rootlets were not included in the same electron microscopic section as in controls, this indicated that about half of the centrioles lacked a basal foot and half lacked a rootlet. Similar results were obtained with *vfl3(RNAi)*, although the defects were less pronounced (52 ± 8 % of

centrioles without a basal foot and 48 ± 6 % without a rootlet visible in the same section; ~ 1/3 of centrioles of each category considering the overestimation due to sectioning). In addition, centrioles with anomalies in the number and/or respective positions of the appendages were observed (Figure 4C, D), suggesting that VFL1 and VFL3 affect the rotational asymmetry of centrioles. Thus, ODF2, VFL1 and VFL3 are centriole components required for appendage formation in the planarian epidermis. How is this related to the chirality of the sidewinder phenotypes? Strikingly, structural chirality is more conspicuous in planarians in which the basal foot is asymmetric and positioned at an angle with respect to the beating axis (Figure 4D), unlike vertebrate basal feet that look more symmetric (Kunimoto et al., 2012; Mitchell et al., 2007). In addition, we noticed a strong left-right bias in cases where the respective positions of appendages were aberrant, as the basal foot was almost always found on the same side of the centriole with respect to the rootlet axis (31/32 of *vfl3(RNAi)* and 10/10 of *vfl1(RNAi)* centrioles were as in Figure 4D-d,e), suggesting that microtubule triplets on the left side possess specific characteristics. Thus, the basal foot and the centriole itself are left-right asymmetric, and these asymmetries depend in part on the ODF2 and VFL1/3 proteins.

ODF2 and VFL1/3 allow organizing a left-right asymmetric centriole network

One plausible model is that centriole chirality affects the architecture of cytoskeletal networks attached to the centrioles, possibly generating left-right asymmetric forces. To better understand how ODF2 and VFL1/3 proteins affect the connections between centrioles, we studied their impact on centriole network organization. In planarians, large mucus granules (up to several microns in diameter) are secreted directly through the surface of the cells (Basquin et al., 2015; Hayes, 2017). Accordingly, we noticed that centrioles were irregularly distributed at the apical surface of control planarians, revealing the presence of “holes” in the pattern that likely correspond to mucus secreting sites (Figure 5A). Outside of these regions however, centrioles tended to align both laterally and along the beating direction, forming rows of up to 10 aligned centrioles (Figure 5A, Figure S6).

Within these rows, the distance separating consecutive centrioles along the two axes showed little variation (Figure 5B), suggesting the existence of structural constraints in centriole network organization. Ultrastructural analyses revealed that rootlets often terminate in the vicinity of a posteriorly positioned centriole and are on average 1.52 ± 0.28 µm long (n = 73), close to the mean longitudinal distance determined by immunofluorescence (Figure 5B, C). Thus, rootlets appear to act as spacers between centriole rows along the beating axis. In addition, we observed microtubules attached to a basal foot and running perpendicular or oblique to the beating axis (Figure 5D), suggesting that microtubules are involved in the lateral alignment of centrioles. Hence these data suggest that cytoskeletal connection between appendages connect neighboring centrioles to achieve proper spacing and alignment, as described in other systems (Kunimoto et al., 2012; Werner et al., 2011).

We next analyzed the impact of ODF2 and VFL1/3-depletion on centriole organization. In *odf2(RNAi)* animals, alignment of centrioles was still detected both longitudinally and laterally in most of the cells, although defects in centriole alignment and polarity were widespread (Figure 5E, F). Thus, centrioles are aligned and spaced apart in a manner that is to a large extent independent from the basal foot, possibly via actin connectors as in *Xenopus* (Antoniades et al., 2014), although we could not observe actin with sufficient resolution in the planarian epidermis. This network induces a clockwise rotation of the centrioles that in control planarians is counteracted by cytoskeletal elements acting on the basal foot. In *vfl1(RNAi)* and *vfl3(RNAi)* animals, centriole alignment was strongly perturbed, indicating a more severe disorganization of the centriole network (Figure 5E, F). This is not unexpected as depletion of VFL1/3 impairs rootlet assembly, and rootlets seem to play a role in the longitudinal organization of centrioles. *vfl1(RNAi)* and *vfl3(RNAi)* animals are also partially defective in basal foot assembly, and hence the counter-clockwise rotation of rootlets observed in these conditions is unlikely to result solely from forces exerted via ODF2 and the basal foot. In agreement with this, the simultaneous depletion of VFL1/3 and ODF2 neither randomized, nor disrupted rootlet patterns (Figure S1, S3, S7; Movie S4), supporting the existence

of additional attachment points between the cytoskeleton and the centrioles (component X in Figure 5G; Figure S7).

Taken together, our results support that ODF2 and VFL1/3 are necessary for organizing the centriole network and balancing the left-right asymmetric forces that likely result from an asymmetric attachment of the centrioles to the cytoskeletal network (Figure 5G).

M/L polarization of centrioles involves partially distinct mechanisms on the left and right sides of the body

Given the intrinsic chirality of the centriole network, how can planarians achieve the bilaterally symmetric rootlet pattern observed in wild type animals? Our recent results demonstrate that the wild-type pattern emerges via the integration of Wnt/PCP and Ft/Ds planar cell polarity cues that act specifically along the A/P and M/L axes, respectively (Vu et al., 2018). Planar cell polarity pathways control the position of cellular structures by interacting with cytoskeletal networks (Devenport, 2014). We reasoned that if the Ft/Ds pathway acts via ODF2 or VFL1/3 to generate the splay observed in control animals, then the implementation of Ft/Ds cues should be hindered when ODF2 or VFL1/3 are missing. To test this, we down-regulated the Wnt/PCP pathway in sidewinder animals. In wild type planarians, depleting DVL1/2 induced rootlet reorientation towards the edges under the influence of the Ft/Ds pathway (Figure 6A, B; Figure S1, S3; Movie S5) (Vu et al., 2018). Although DVL1/2 is involved in additional pathways, in particular the Wnt/β-catenin pathway, this phenotype is most likely to result from a decrease in Wnt/PCP signaling (Vu et al., 2018).

In VFL1 and VFL3-depleted animals, Wnt/PCP down-regulation induced rootlet reorientation like in control animals on the left side and to a lesser extent on the right side, suggesting that centrioles could still detect the Ft/Ds polarity field. In *odf2(RNAi)* animals, dampening Wnt/PCP activity induced a markedly asymmetric response: centrioles reoriented on the right side to a similar extent than in control planarians but failed to do so on the left side (Figure 6A, B; Figure S3). This suggested that on the left side the centriole network no longer aligned in the Ft/Ds polarity field,

even when its relative influence was increased by Wnt/PCP inhibition. In contrast, re-polarization on the right side of *odf2;dvl1/2(RNAi)* planarians indicated that Ft/Ds cues were still implemented, and hence the possibility that ODF2 is not required for rootlet splay on this side of the body. If this were the case, simultaneous depletion of ODF2 and the Ft/Ds pathway should produce a uniform rootlet orientation along the M/L axis. However, we found no significant difference between *odf2(RNAi)* and *odf2;ds(RNAi)* animals in this respect (Figure 6C, D; Figure S1, S3), suggesting that the response to Ft/Ds is impaired on both sides of the epidermis when ODF2 is missing. Together, these observations suggest that the rootlet pattern observed in *odf2(RNAi)* animals results from a defect in centriole network structure super-imposed with a defect in the response to Ft/Ds cues. On the left side, the clockwise rotation of centrioles driven by VFL1/3-dependent connections is compensated by the lack of response to Ft/Ds, resulting in rootlet angles that are close to control values (Figure 2A-C; Figure S3). On the right side, the defects in network architecture and in the response to Ft/Ds both induce a clockwise rotation of centrioles, leading to a strong deviation from control values. In addition, the data obtained after a simultaneous inhibition of DVL1/2 and ODF2 supports that a distinct mechanism can drive centriole repolarization in response to Ft/Ds cues on the right side of the epidermis.

Altogether, our results support that ODF2 is required for the M/L polarization of centrioles in the planarian epidermis, most likely via its role in basal foot assembly. Additional components of the centriole network contribute specifically on the right side, supporting that the mechanism underlying M/L polarization is implemented differentially on each side of the midline (Figure 7).

Discussion

This work illustrates how a bilaterally symmetric whole-tissue pattern can emerge from a prominently asymmetric cellular structure. In the multiciliated epidermis of planarian flatworms, centrioles are organized into an asymmetric mirror-imaged medio-lateral pattern, a property that likely derives from their intrinsic chirality. This network is polarized to generate a bilaterally symmetric pattern via a mechanism that is executed differentially on the left and right halves of the epidermis, reflecting the asymmetric nature of the network itself. We show that the centriole components ODF2, VFL1 and VFL3 are required for establishing chiral asymmetric connections between centrioles and balancing their effects. These proteins act in part by controlling the assembly of the basal foot, which in planarians has a structure that mirrors centriole chirality. Organizing chiral asymmetric cytoskeletal arrays is likely an ancestral property of centrioles (Yubuki and Leander, 2013), and this property is thus conserved in some metazoan species.

Functions of the ODF2 and VFL1/3 proteins and balance-of-force model of centriole orientation

The centriole network organized in part via ODF2 and VFL1/3 proteins is inherently asymmetric, independently of M/L polarity cues. This is best illustrated at the midline and the posterior end, where M/L polarity cues have a limited effect, but rootlets are nevertheless deviated from the A/P axis in RNAi animals. Network asymmetry likely stems from an asymmetric attachment of cytoskeletal elements to centrioles mediated by ODF2 and VFL1/3. Our results show that planarian ODF2 and VFL1/3 are required for building centriole appendages, which are known to organize cytoskeletal connectors necessary for positioning the centrioles in multiciliated cells (Antoniades et al., 2014; Clare et al., 2014; Kunimoto et al., 2012; Werner et al., 2011). ODF2 is necessary to basal foot assembly, consistent with results obtained in mouse (Kunimoto et al., 2012) thus establishing the evolutionary conservation of this function. The roles of VFL1 and VFL3 appear more complex but these proteins also affect the assembly and position of the basal foot, as well as of the ciliary

rootlet. These findings are reminiscent of studies in unicellular eukaryotes showing that VFL1/3 orthologs are required for building different sets of striated fibers and microtubule rootlets specific to each species (Adams et al., 1985; Bengueddach et al., 2017; Silflow et al., 2001; Wright et al., 1983). Hence, the functions of these proteins appear conserved despite important variations in the architecture of centriole-associated structures. In unicellular models, orthologs of VFL1 and VFL3 localize to specific microtubule triplets (Bengueddach et al., 2017; Silflow et al., 2001). In planarians, absence of VFL1 or VFL3 lead to basal feet assembling on the wrong triplets, most of the time shifting one triplet to the left. This suggests that VFL1/3 proteins might normally help restricting basal foot assembly to its proper site between the triplet facing the direction of beating and the triplet placed immediately to its left. Moreover, the striking differences between the *vfl1/3(RNAi)* and *odf2(RNAi)* phenotypes support that VFL1/3 proteins play an additional role beyond appendage assembly. When ODF2 was missing, VFL1/3-dependent forces rotated centrioles clockwise. In *Xenopus*, actin cables anchored in the vicinity of the basal foot connect centrioles laterally and contribute to centriole spacing (Antoniades et al., 2014). Centriole spacing is mostly unaffected in *odf2(RNAi)* but is perturbed in *vfl1/3(RNAi)*, suggesting that VFL1/3 proteins might connect centrioles to the actin network. One possible model is that VFL1/3 anchor actin filaments in an asymmetric fashion to one or more triplets localized on the left of the basal foot. This would be consistent with the clockwise rotation of centrioles observed when ODF2 is missing. In the presence of ODF2, the rotation induced by VFL1/3-dependent connections is compensated, possibly by microtubules anchored at the basal foot and running perpendicular to the beating axis that we indeed observed. How these microtubules generate a left-right asymmetric net force is unclear, but one possibility is that their orientation is biased along the M/L axis. The basal foot in planarians has an asymmetric shape, which might affect the polarity of microtubules attached to it. Beyond VFL1/3 and ODF2, additional players are also involved, as depletion of all three proteins is not sufficient to randomize centriole rotational polarity in this system (Figure 7). In wild type

planarians, the forces exerted by the different network components are balanced, thus compensating centriole chirality and masking the asymmetry of the network.

Interaction of the centriole network with M/L polarity cues to generate bilateral symmetry

In addition to its role in organizing the network of centrioles, our analyses support that ODF2 is key to implementing the M/L polarity cues generated by the Ft/Ds pathway. Indeed, depletion of Ds produced no additive effect in *odf2(RNAi)* planarians, indicating that Ft/Ds pathway is already ineffective when ODF2 is down-regulated. Microtubules anchored at the basal foot might orient centrioles towards the body edges (Figure 7), in line with the role played by the Ft/Ds pathway in polarizing microtubule networks in other systems (Matis et al., 2014). Further work is required to test this model and exclude alternative possibilities, for instance that Ft/Ds acts downstream or in parallel to ODF2. Analysis of *odf2;dvl1/2(RNAi)* animals nevertheless supports that M/L polarization can rely on additional network components on the right side of the body, as centriole re-polarized towards the right edge under the influence of M/L cues to a similar extent than in controls (Figure 7). Hence, the bilaterally symmetric pattern of centrioles observed in the planarian epidermis results from interactions between polarity cues and the cytoskeleton that are at least partly distinct on each side of the body. Why this did not result in a quantitative difference between the *odf2(RNAi)* and *odf2;ds(RNAi)* phenotypes is unclear, but one possibility is that the repolarization driven by ODF2-independent cytoskeletal arrays was enhanced by DVL1/2 down-regulation and thus easier to detect in these conditions.

Biological significance of network asymmetry

Our results support that centriole network asymmetry originates from asymmetries within the centrioles. Centrioles are intrinsically chiral structures, and this property is amplified in many unicellular eukaryotes by the presence of appendages that decorate specific microtubule triplets. In planarians, the basal foot is left/right asymmetric, and the *vfl1/3(RNAi)* phenotype points at

additional asymmetries between microtubule triplets. Whether the polarization mechanism we uncovered is essentially required to compensate centriole chirality, or whether it allows generating larger-scale chirality remains an open question, however. Whole-cell chirality, which stems from inherent properties of the cytoskeleton, is widespread in animals (Kuroda et al., 2009; Wan et al., 2011; Xu et al., 2005). In some systems, whole-cell chirality has been linked to the establishment of left-right asymmetry of the body plan (Kuroda et al., 2009; Taniguchi et al., 2011). Planarians have no clear left/right asymmetry in this respect, but structural chirality in the epidermis might contribute generating the complex pattern of centrioles, reflecting the ancestral role of centrioles in shaping elaborate cell geometries. Future work will tell whether this mechanism evolved with the dual-axis control of planar polarity in planarians epidermis or whether it reflects a fundamental property of centriole networks.

Acknowledgements

The authors would like to thank L. Kodjabachian for critical reading of the manuscript, and P. Le Gars and M. K. Nguyen for technical help. We acknowledge the ImagoSeine facility, member of the France BioImaging infrastructure supported by grant ANR-10-INSB-04 from the French National Research Agency. **Funding:** This work was supported by CNRS (ATIP-AVENIR) and ANR (ORICEN) funding to J.A. N.G. was recipient of a MESRI PhD fellowship from the French Government. D.E. was funded by the European Research Council (Cog forecaster n°647073).

Authors contributions

Conceptualization, C.B., D.E., J.C.R. and J.A.; Methodology, C.B., D.E., B.L. and J.F.P.; Investigation, C.B., D.E., H.T.V., B.L., J.F.P., A.M.O. and J.A.; Resources: N.G., S.M., H.T.V. and J.C.R.; Writing, C.B., J.C.R. and J.A.

Declaration of interests: The authors declare no competing interests.

Main figure titles and legends

Figure 1. Depletion of SMED-ODF2 and SMED-VFL1/3 affect the direction of locomotion in an opposite manner. **(A)** *t*-projection (2 s apart) of control planarians or animals depleted from VFL1/3 and ODF2. Black arrows: expected trajectory based on the initial orientation of the A/P axis; White arrows: observed trajectory. Red arrowheads: position of the head. Bar is 1 mm. **(B)** Quantification of the angle between the translocation and head-tail vectors as shown in (A). 3 independent experiments, $62 \leq n \leq 344$ for each condition. Error bars represent SD. Asterisks indicate a significant difference from the control condition (Kruskal-Wallis test; $^{***}p < 0.001$). **(C)** Locomotion speed of control and RNAi animals. 3 independent experiments, $41 \leq n \leq 120$ for each condition. Error bars represent SD. Asterisks indicate a significant difference from the control condition (Kruskal-Wallis test; $^{*}p < 0.05$, $^{**}p < 0.01$, $^{***}p < 0.001$). **(D)** Ciliary beat frequency in control and RNAi animals. $11 \leq n \leq 26$ independent measurements were performed on a total of 2 (control) or 3 (RNAi) different animals. Error bars represent SD. Asterisks indicate a significant difference from the control condition (Kruskal-Wallis test; $^{*}p < 0.05$). **(E)** Immunofluorescence views of the ventral epidermis of control and RNAi planarians. Centrioles were stained with an anti-SMED-CEP135 antibody (red) and cilia with an anti-acetylated tubulin (green). Bar is 5 µm. See also Figure S1 and Movie S1, S2.

Figure 2. Sidewinder locomotion phenotypes are caused by aberrant centriole rotational polarity in the ventral epidermis. **(A)** Graphical representation of rootlet angle variation along the M/L axis in the anterior and posterior sides of control and RNAi planarians. Individual curves represent a single animal except the red curve that shows the mean. **(B)** Centriole rotational polarity in the ventral epidermis of control or RNAi animals (viewed from above). Arrows show the orientation of the mean rootlet angle vector for each of 200 subdivisions of the epidermis. The color

code highlights the CW (blue) or CCW (red) rotation of rootlets with respect to the A/P axis. $n \geq 6$ animals per condition. **(C)** Heatmap of the local circular standard deviation (CSD) values associated to the mean rootlet angles represented in (B). The mean of all local CSD values is also indicated. $n \geq 6$ animals per condition. **(D)** Schematic representation of angle deviations induced by depletion of VFL1/3 and ODF2. In each quadrant, arrows show the mean rootlet angle in control (black arrow) or RNAi-treated (gray arrow) planarians. Angle deviations are color-coded and the corresponding numeric value are indicated. See also Figure S1, S3.

Figure 3. Rootlet orientation defects in RNAi planarians are sufficient to predict sidewinder locomotion. **(A)** Simulation of trajectories of control and RNAi planarians based on experimentally measured rootlet angles (see STAR Methods). The position of the head is in yellow. Red crosses at x,y(0,0) indicate the starting point (t = 0) and black arrows show the direction of locomotion. **(B)** Simulation of trajectories over longer time scales using experimental data obtained from *vfl1*-, *vfl3*-, *odf2*- or control RNAi animals. The model predicts that depletion of VFL1, VFL3 and ODF2 will all result in a CW circular trajectory. For each graph, the anterior pole of the planarian is in yellow, the red cross at x,y (0,0) indicates the starting point (t = 0) and the black arrow shows the direction of locomotion. **(C)** Experimental observation of the CW circular trajectories of *vfl1*-, *vfl3*- and *odf2(RNAi)* animals over longer time scales (~ 2 minutes). Each image corresponds to a *t*-projection of individual frames taken 5 seconds apart. Animals fortuitously crossing the field of acquisition (see Movie S3) were manually erased for improved clarity. Red arrowheads indicate the head of the planarian at the beginning of the movie. Bar is 5 mm. See also Figure S4 and Movie S3.

Figure 4. ODF2 and VFL1/3 are required for proper assembly of centrioles appendages. **(A)** Assessment of anti-SMED-ODF2 and anti-SMED-VFL1 antibody specificity by Western blot. Anti-SMED-CEP135 and anti-acetylated tubulin were used as loading controls. 50 µg total proteins

(10 µg for acetylated-tubulin) from control, *odf2(RNAi)* and *vfl1(RNAi)* samples were analyzed. **(B)** Immunofluorescence views of the ventral epidermis showing the respective localization of ODF2 (top) or VFL1 (bottom) in red and ROOTLETIN1 in green. Insets are magnified x 5. Bars are 5 µm (insets: 1 µm). **(C)** Quantification of centriole ultrastructural defects in the ventral epidermis of control or RNAi animals. Percentages of centrioles with a basal foot and a rootlet at the correct position (1), no visible basal foot (2), no visible rootlet (3), no visible appendage (4) or appendages in abnormal number and/or relative positions (5) are shown. For each condition, 300-500 centrioles from 2-3 different animals were analyzed. Bars represent SD between different animals. **(E)** Electron microscopic views of centrioles in epidermal cells in control (a), *odf2(RNAi)* (b) or *vfl3(RNAi)* (c-e) animals. Bar is 0.2 µm. See also Figure S5.

Figure 5. ODF2 and VFL1/3 organize a left-right asymmetric network of centrioles. (A) ROOTLETIN1 staining of the ventral epidermis of a control animal. White line on the right panel: cell boundary; red circles: putative mucus secretion sites. Orange and blue lines: longitudinal and lateral rows of centrioles, respectively. Bar is 5 µm. **(B)** Mean distance separating neighboring centrioles in lateral and longitudinal rows in control animals ($n \geq 700$ measurements from 17 different animals). Bars represent SD. Asterisks indicate a significant difference between the two variables (Mann-Whitney test; $^{***}p < 0.001$). **(C)** Electron microscopic view of a control multiciliated cell showing a longitudinal row of centrioles. Red arrowheads point at rootlet tips. Bar is 0.5 µm. **(D)** Electron microscopic view of an epidermal centriole. Arrowheads highlight a microtubule in the vicinity of two basal feet. Bar is 0.1 µm. **(E)** ROOTLETIN1 staining of the ventral epidermis of RNAi animals. Bar is 5 µm. **(F)** Percentage of epidermal cells displaying at least one rectangular arrangement of minimum four centrioles ($n \geq 500$ cells from 5 different animals analyzed per condition). Bars represent SD. Asterisks indicate a significant difference from the control condition (Kruskal-Wallis test; $^{*}p < 0.05$, $^{**}p < 0.01$). **(G)** Schematic model of the

organization of centrioles in planarian multiciliated cells and the forces exerted on individual centrioles by elements of the cytoskeletal network via VFL1, VFL3 or ODF2 in control and RNAi-depleted planarians. The involvement of a component X is supported by results from the simultaneous inactivation of VFL1/3 and ODF2. The exact position where cytoskeletal elements bind to centrioles via VFL1/3- and X, and the notion that all forces are pulling forces, are hypothetical. See also Figure S1, S6, S7 and Movie S4.

Figure 6. M/L polarization of centrioles requires ODF2 and additional network components. **(A)** Centriole rotational polarity in flatworms depleted from DVL1/2 only or in combination with depletion of VFL1, VFL3 or ODF2, represented as in Figure 2B ($n \geq 5$ animals analyzed per condition). **(B)** Schematic representation of the shift resulting from DVL1/2 depletion in control and RNAi animals. Arrows: mean rootlet orientation in each quadrant in the presence of normal (black arrows) or decreased (gray arrows) levels of DVL1/2. Angle deviations between control and RNAi-treated animals are color-coded and the corresponding numeric value are indicated. **(C)** Centriole rotational polarity in *ds(RNAi), odf2(RNAi)* or *odf2;ds(RNAi)* planarians as in (A) ($n = 4$ for *ds(RNAi),* 2 for *odf2(RNAi)* and 6 for *odf2;ds(RNAi)*). **(D)** Schematic representation of angle deviations resulting from Ds depletion in ODF2-depleted animals as in (B). See also Figure S1-S3 and Movie S5.

Figure 7. Proposed model for M/L polarization of centrioles on each side of the ventral epidermis. The chiral asymmetric centriole network resulting from the balanced action of ODF2 and VFL1/3 (represented as in Figure 5G) is polarized by a mechanism that is executed in a differential manner on the left and right sides of the body: on the left side, polarization depends on ODF2, possibly acting downstream of the Ft/Ds pathway (in green), whereas on the right side it involves both ODF2 and other network components.

STAR Methods

Lead contact and materials availability

Further information and requests for resources and reagents should be directed to and will be fulfilled by the Lead Contact, Juliette Azimzadeh (juliette.azimzadeh@ijm.fr). All unique reagents generated in this study are available from the Lead Contact with a completed Materials Transfer Agreement.

Experimental Model and Subject Details

Asexual *Schmidtea mediterannea* (strain CIW4) (Sanchez Alvarado et al., 2002) were maintained in the dark at 20 ºC in plastic containers filled with 1 X Monjuic water (1.6 mM NaCl, 1 mM $CaCl_2$, 1 mM $MgSO_4$, 0.1 mM $MgCl_2$, 0.1 mM KCl, 1.2 mM $NaHCO_3$, pH 7.2) and fed weekly with calf liver homogenate (Basquin et al., 2015). Animals were starved one week prior to experiments.

Methods details

RNA interference

ODF2, VFL1, VFL3 cDNAs cloned in pPR-T4P were described in (Azimzadeh et al., 2012), DVL1 and DVL2 in (Gurley et al., 2008). *Caenorhabditis elegans* UNC22 cloned in pPR-T4P (Liu et al., 2013) was used in all control experiments. Production and RNAi feeding was performed as described in (Basquin et al., 2015). Briefly, constructs were transformed into competent *Escherichia coli* strain HT115 (Timmons et al., 2001). Bacteria were grown in 2XYT medium, induced with 0.1 mM IPTG during 2 hours, pelleted and mixed with calf liver (1:0.66:1.34 bacteria: 1 X Montjuic water: calf liver homogenate). ~1 cm long animals were fed three times two days apart and

amputated pre- and post-pharyngeally the day after the last feeding. Planarians were then fed once a week at least twice more before being processed for experiments. For simultaneous inactivation of 2 or 3 genes, bacteria/liver mixes for control or specific target genes were used at 1:1 or 1:1:1 ratios, respectively.

Antibodies

Rabbit polyclonal antibodies directed against SMED-VFL1 and SMED-ODF2 proteins were developed in the laboratory. Fragments corresponding ODF2 a.a. 599-769 (based on SmedGB sequence SMU15005577) (Robb et al., 2015) and VFL1 a.a. 575-703 (SMU15036303) were amplified by RT-PCR, cloned in pGST-Parallel1 and expressed in *Escherichia coli*. Bacterial pellets were solubilized in TNE buffer (50 mM Tris pH 7.5, 150 mM NaCl, 1 mM EDTA) containing 5 mM DTT, 20 mg/mL Lysozyme, 0.25 % sodium deoxycholate, 250 U/mL DNAse I, 5 mM $MgCl_2$ and protease inhibitor cocktail (Roche). The lysates were cleared out by centrifugation at 15,000g before incubation with Glutathione Agarose beads (Thermofisher Scientific). The beads were washed 5 x with 50 mL TNE buffer containing 0.1 % Triton X-100, and the protein fragments were recovered by overnight incubation with 75 µg Tobacco Etch Virus protease in 1.5 mL TNE buffer supplemented with 5 mM DTT. The supernatants containing the cleaved protein fragments were then dialyzed against PBS before rabbit immunization (Covalab France). Antibodies were affinity-purified on the corresponding antigen immobilized on Affi-Gel 10 resin (Bio-Rad Laboratories). For this, 1-3 mg soluble antigen diluted in 0.1 M MOPS buffer pH 7.5 containing 0.1 M NaCl were incubated overnight at 4 °C with 1.5 mL Affi-Gel 10 beads activated following the manufacturer's recommendations. The beads were then incubated with 5 mL rabbit antiserum diluted 5 x in PBS, transferred to a Poly-prep chromatography column (Bio-Rad) and washed with 80 mL PBS at 4 °C. Immunoglobulins were recovered by elution with 0.1 M Glycine pH 2.2 followed by neutralization with Tris base (100 mM final concentration), dialyzed against PBS

buffer containing 50 % glycerol and stored at – 20 °C. The anti-SMED-ROOTLETIN1 was described in (Vu et al., 2018) and the anti-SMED-CEP135 antibody in (Azimzadeh et al., 2012).

Whole mount Immunofluorescence

~ 0.1 - 0.3 cm long animals were euthanized in 1 % HCl during 1 min, fixed overnight at RT in methanol then rehydrated in graded series of methanol: 75%, 50%, 25% methanol in Montjuic water. Non-specific antibody binding sites were blocked 4 hours in PBS containing 2.5 % BSA and 0.5 % Tween-20 (PBST), and samples were incubated overnight at 4 °C with primary antibodies at the following dilutions: anti-SMED-ROOTLETIN1 (1:500), anti-SMED-VFL1 (1:3000), anti-SMED-ODF2 (1:300) and anti-SMED-CEP135 antibody (1:500). DyLight488/550 secondary antibodies (Thermofisher Scientific) were used at a dilution of 1:300. Samples were washed 4 x during 1 hour in PBST and incubated 4 hours at RT with secondary antibodies, Concanavalin A coupled to AlexaFluor 647 (1:300; Thermofisher Scientific) to label membranes (Zayas et al., 2010) and 5 µg/mL Hoechst 33342 to label nuclei. Samples were washed 4 x during 1 hour in PBST and mounted in Vectashield (Vector laboratories). For analysis of the *ds;odf2(RNAi)*, 0.8-1 cm long animals were used because the *ds(RNAi)* phenotype is more penetrant in larger animals. The flatworms were anaesthetized in cold 0.2% chloretone in planarian water until completely stretched out, positioned on a filter paper on a cold block with their ventral side up and fixed with ice-cold methanol for at least 1 hour at - 20 °C. The samples were then bleached in 6% H_2O_2 in methanol overnight under direct light, gradually rehydrated to PBS with 0.1 % Triton X-100 (PBSTw0.1%), transferred into reduction solution (1 % NP40, 50 mM DTT and 0.5 % SDS in PBS) for 10 minutes at 37 °C, followed by 2 x 10 minute washes with PBSTw0.1%. The samples were then blocked for 1 hour in 10 % filtered horse serum in PBSTw0.1%, followed by primary antibody incubation in blocking solution (anti-SMED-ROOTLETIN-1 1:500, and anti-SMED-CEP135 1:500) overnight at 4 °C. The samples were washed 6-8 times for 4 hours in PBSTw0.1%, and then incubated in

secondary antibody in blocking solution (both secondary antibodies were used at 1:500) for 4 hours at room temperature (or overnight at 4 °C). Stained samples were washed 4-6 times for 2 hours in PBSTw0.1%, and then mounted in 80 % glycerol (prepared in 10 mM Tris pH 8.5).

qPCR

Total RNA extracts were obtained using TRI-Reagent (Molecular Research Center) and cDNAs were synthetized using SuperScript III reverse transcriptase (Thermofisher Scientific). qPCR was performed with GoTaq qPCR Master Mix (Promega) and the primers referenced in Table S1 in a LightCycler 480 instrument (Roche). Quantification of relative mRNA levels was performed using 3 reference genes (smed-chmp2a, smed-emc7, and smed-ura4) following the MIQE guidelines (Bustin et al., 2009).

Image acquisition and analysis

The ventral epidermis of planarians was imaged on an inverted Axio Observer Z.1 microscope (Zeiss) equipped with a sCMOS Orca Flash4 LT camera (Hamamatsu) using an air 10x objective (Plan Apo, N.A. 0.45) or an oil 63x objective (Plan Apo, N.A. 1.4). For rootlet analysis, optical sections were acquired at a 0.24 µm interval using the 63 x objective and tiled images were stitched using ZEN software (Zeiss). Signal was enhanced using Subtract Background plugin and z-stacks were submitted to maximum intensity projection using ImageJ software (Schneider et al., 2012). To obtain rootlet polarity and position, vectors were drawn manually for each rootlet from the centriole-attachment side (bright end) to the tip of the comet using ObjectJ Plugin (Vischer et al., 2015). The contour of planarians was determined on images acquired with the 10 x objective and the midline was positioned at equal distances of the lateral boundaries. The position of each rootlet relative to the M/L and A/P axes was determined. Planarians were segmented in 2 or 10 M/L and 2,

5 or 20 A/P segments, then mean rootlet orientation and circular standard deviation were calculated for each subdivision. For analysis of the *ds;odf2(RNAi)*, we used the automatic pipeline described in (Vu et al., 2018) because large specimens are difficult to analyze manually. *odf2(RNAi)* animals were re-analyzed in parallel to verify that it produces similar results as manual analysis of smaller specimens. *ds(RNAi)* planarians were also analyzed in the same experiment to confirm the efficiency of Ds-depletion.

Live imaging

Live animals were imaged at 10 frame.sec^{-1} using a M205C stereomicroscope equipped with a 0.63 x objective (PlanApo) and DFC450 camera (Leica), or a PowerShot SX 230 HS camera (Canon) for analysis at longer time scales. The direction of locomotion was determined using ImageJ software by measuring the angle between the planarian A/P axis and the trajectory of the planarians (measured between the photoreceptors). Time sequences (≥ 2 seconds) during which the planarian body remained straight were used for this analysis. To better visualize the trajectories of the planarians shown in Figure 3, animals fortuitously passing in the field were erased manually before projecting consecutive time frames on a single image. For high speed imaging of ciliary beat, live planarians were mounted in a chamber obtained by cutting a ~ 2 x 2 mm square from a parafilm spacer placed between a microscopy slide and an 18 x 18 mm coverslip (Basquin et al., 2015), and were observed on an Axiovert 200 inverted microscope (Zeiss) using an oil immersion x 100 objective. The beating of cilia located at the anterior margin were recorded with a digital camera (PixeLINK A741) at a rate of 355 frames per second as described previously (Papon et al., 2012).

Transmission Electron Microscopy

Planarians were dissected in 4 % paraformaldehyde, 2 % glutaraldehyde in 0.1 M cacodylate pH 7.4 and fixed 4 x 1 minute in a Model 3450 Microwave Oven (Ted Pella Inc.) at 150 W, then incubated 48 hours at 4 °C in 3 % glutaraldehyde in cacodylate buffer. The specimens were next fixed in 1 % OsO4 in cacodylate buffer in the microwave (2 x 1 minute at 150 W, then 6 x 20 seconds at 450 W) and incubated during 1 hour at room temperature. *En bloc* staining was performed by incubating the samples in 0.5 % uranyl acetate overnight at 4 °C. Dehydration was performed using graded series of 35, 50, 75, 80, 95, 100 % ethanol in water. Samples were rinsed in acetone and infiltration was performed using graded series of 10-100 % epon/araldite resin (Ted Pella Inc.) in acetone with 10 % increments, 4 x 1 minute in the microwave at 350 W for each concentration. Samples were incubated overnight in 100 % resin and then 4 hours in resin with accelerant before embedding. Ultrathin sections were obtained using an EM UC6 Ultracut microtome (Leica), stained with uranyl acetate and lead citrate, and examined in a Tecnai 12 transmission electron microscope (Thermofisher Scientific).

Computational modelling

To test the hypothesis that orientation of the cilia can ultimately determine the movement phenotype of a planarian as a whole, we devised a simple model that can predict planarian movement based on experimentally observed spatial and angular distributions of cilia within planarians using MATLAB (MathWorks).

We simulate a planarian as a solid body, meaning that there is no deformation of the body (*i.e.* no stretching or bending): the body is translated and rotated as one solid unscalable entity. A body has a rectangular shape and is divided, as in our experiments, into segments; the head and the tail have the same geometry (Figure S4A). We can arbitrarily set the length (L), the width (W) and the mass (M) of the whole body; the number of segments along L and W, from which the mass and the

size of a single segment is then calculated. Each segment comprises a number of nodes (red circles in Figure S4A) that represent rootlets of cilia, and with each node cilia a beating force is associated during simulations. The number of nodes N in each segment is drawn randomly from a normal distribution, the mean and the standard deviation of which we control (N_m, N_s in Figure S4A). Spatial distribution of these N nodes within a segment is uniform: there is no spatial bias and a node can be placed anywhere inside the segment with the same probability. The parameters described above (planarian mass, length, width; segment mass, length, width, number; nodes numbers and spatial distribution) are fixed during generation of a planarian and do not change during simulation runs. Ideally, one segment should represent one cell with its unique spatial configuration of nodes. In our simulations, we construct a planarian so that its segments conform to our experimental planarian segmentation: 5 segments along the A/P axis and 10 segments along the M/L axis. However, this is absolutely not necessary to reproduce our simulation results. During each simulation iteration nodes in all segments individually generate a force due to cilia beating; these forces vary in direction and magnitude. Therefore, we associate with each node the angle of the beating force and its absolute magnitude f; their values will be drawn from normal distributions, the mean and the standard deviation of which we control (Figure S4B). The angle is counted clock-wise from the Tail-Head axis for positive angles and counter clock wise for negative. We also introduce notation of incoherency in cilia beating: at any given iteration, there is only a fraction of segment's nodes (φ_{on}, varies from 0 to 1) that have beating cilia and thus are "on" (s = 1, red nodes), whereas the other segment's nodes ($1 - \varphi_{on}$) have resting cilia and are "off" (s = 0, blue nodes). Thus, when $\varphi_{on} = 1$, cilia beating is fully coherent and all cilia beat together during an iteration. The fraction of nodes with beating cilia φ_{on} is drawn from a normal distribution, the mean and the standard deviation of which we control (Figure S4B). These three normal distributions (α, f, and φ_{on}) are constructed during generation of a planarian, apply to all segments within this planarian and do not change during simulation runs. During new iteration, each segment acquires a new configuration of

beating cilia by drawing randomly parameters α, *f*, and *s* for each node from these distributions; each node is first set to "off" state and then turned "on" with the probability of φ_{on}. Some parameters can be found experimentally: the planarian sizes (L, W); normal distributions for drawing the number of nodes per segment (N) and the angular distribution of beating forces (α) (may be found experimentally in each segment as in Figure 2B). Some we set arbitrarily: the planarian mass (M), the magnitude distribution of the beating force (*f*) and the probability of on-off state (φ) are set arbitrarily.

We define planarian movement as a combination of translation of the whole body and rotation around its center of mass M (Figure S4D). To find the translation, we first calculate the total force $\vec{F}$ generated by all beating cilia in the planarian (in all segments at each node); since the planarian is modeled as a rigid body, all cilia beating forces may directly be applied to the center of mass M. We then model the experimentally observed constant speed movement of planarians as follows. We assume that during each infinitesimal time span Δt the planarian speed starts from 0, accelerates due to action of $\vec{F}$ and decelerates back to 0 due to action of counter forces (*e.g.* friction). More specifically, in the first half (from 0 to $\Delta t/2$) acceleration is $a = F/M$ (according to second Newton's law), and during the second half (from $\Delta t/2$ to Δt) deceleration is $a = -F/M$ (we use symmetric evolution of the speed for simplicity of calculations). Such periodic movement can be approximated as movement with constant speed $V = \frac{F\Delta t}{4M}$. Thus, we can calculate the translation from old position p_0 to new position p during iteration time Δt as

$$\vec{p} = \vec{p}_0 + \frac{\vec{F}}{4M}\Delta t^2 \qquad (1)$$

To find the rotation, we calculate for each i_{th} segment the net force $\vec{F}_i$ arising from all its beating cilia and the torque $\vec{T}_i = \vec{r}_i \times \vec{F}_i$ about the planarian's center of mass M that $\vec{F}_i$ generates (Figure S4C). The total torque of the planarian $\vec{T}$ is then calculated as the sum of all $\vec{T}_i$. According to

Euler's second law: $\frac{\Delta\omega}{\Delta t} = \frac{\vec{T}}{I}$, where $\frac{\Delta\omega}{\Delta t}$ is the angular acceleration, $\omega = \frac{\theta}{\Delta t}$ is the angular speed, $I = \sum_i {r_i}^2 m_i$ is the moment of inertia of the planarian body with r_i and m_i is the position and the mass of the i_{th} planarian segment. Following the same considerations as in the case of translation, we can approximate planarian's rotation as rotation with constant angular speed $\omega = \frac{T\Delta t}{4I}$. Thus, we can calculate the rotation from old angle θ_0 to new angle θ during iteration time Δt as

$$\theta = \theta_0 \pm \frac{T}{4I}\Delta t^2 \qquad (2)$$

where the sign depends on the direction of the torque.

In each new iteration, all segments acquire new cilia beating configuration, after this new total force $\vec{F}$ and total torque $\vec{T}$ are calculated; then using equations (1) and (2) new position and new body orientation $(\vec{p}, \theta)$ are calculated.

Order of events in the simulation

- Planarian generation. Parameters of the planarian:
    - Body mass (M), length (L) and width (W), initial orientation (in Figure S4 orientation is 90 degrees).
    - Segment numbers along body length and width N_L, N_W.
    - Node number bias; mean and standard deviation (N_m, N_σ).
    - Cilia beating angle bias; mean and standard deviation (α_m, α_σ).
    - Cilia beating force strength bias; mean and standard deviation (f_m, f_σ).
    - Cilia beating coherency bias; mean and standard deviation (φ_m, φ_σ).
    - Segment mass is calculated, node positions are set, cilia beating angles and forces are set, on/off state of each node is set.
- Simulation starts.

- Iteration starts. Node positions never change.
- Cilia beating angle changes randomly within the given bias.
- Cilia beating force changes randomly within the given bias.
- Cilia beating coherency is used to set randomly a fraction of nodes in off state.
- In each segment the total cilia beating force and torque is calculated.
- Total force and torque acting on the whole planarian body is calculated
- The whole body is moved according to the calculated force.
- The whole body is rotated according to the calculated torque.
- Repeat the iteration.

To test the simulation framework and see whether the results are qualitatively consistent, we run several simple tests. First, we generate two planarians: one is biased to rotate left (Figure S4E, planarian 2, with orange segment) and the other is biased to rotate right (planarian 1, with blue segment). All their segments have nodes generating force straight forward (grey segments), except for the colored two that have directional bias. Their trajectories are, as expected, mirrored, as shown with trajectory evolution and body orientation in Figure S4E. Second, we generate several planarians with the same shape parameters, but one without noise and the rest with random noise; their trajectory evolution and body orientation (Figure S4F) show the effect of noise. Varying and even opposite direction of rotation is caused by random asymmetrical distribution of nodes throughout the planarian body (which is fixed after a planarian has been generated), whereas the noise (visible in body orientation curves) comes from random cilia beating direction, force and on/off state. Next, we generate planarians with exactly the same angular bias of cilia per segment as in the experimentally observed RNAi treated animals and run simulations on them. Our framework allows us qualitatively reproduce both linear translation on short time scale and circular movement on longer time scale (Figure 3); the direction of translation and rotation are properly captured as

well. Interestingly, even though these mutants translate in opposite directions, they both circle (rotate) in the same direction. However, it is not possible to quantitatively reproduce the speed of rotation or the speed of translation with simple model; it allows only qualitative translation of experimentally observed angular distributions into trajectories.

Quantification and statistical analysis

Statistical analysis was performed using Oriana 3 (Kovach Computing Services) for comparison of local rootlet angle variation. Significance was determined using Watson-Williams test and was defined as $P \geq 0.05$. All the other analyses were done with Prism 7.0.d (GraphPad). Significance was determined using Kruskal-Wallis test followed by Dunn's multiple comparisons test or with Mann-Whitney test. Statistical details can be found in the legends. Significance was defined as $P \leq 0.05$ ($^{*}p < 0.05$, $^{**}p < 0.01$, $^{***}p < 0.001$). *n* numbers are biological repeats and measurements are represented as mean ± SD.

Data and code availability

The code for computational modelling of planarian locomotion generated during this study is available from the GitHub source-code hosting facility (https://github.com/dershoff/simulation-of-planarian-movement).

Supplemental Videos

Movie S1, related to Figure 1.

Locomotion phenotypes of control, *odf2(RNAi)*, *vfl1(RNAi)* and *vfl3(RNAi)* planarians.

Speed is accelerated 5 times, bar is 1 mm.

Movie S2, related to Figure 1.

High-speed imaging of cilia beating in control, *odf2(RNAi)* and *vfl1(RNAi)* planarians.

Left: control; middle: *odf2(RNAi)*; right: *vfl1(RNAi)*.

Movie S3, related to Figure 3.

Locomotion phenotypes of *odf2(RNAi)*, *vfl1(RNAi)* and *vfl3(RNAi)* planarians at longer time scales.

Speed is accelerated 10 times, bar is 5 mm.

Movie S4, related to Figure 5.

Locomotion phenotypes of planarians simultaneously depleted from two or all three sidewinder genes.

Speed is accelerated 5 times, bar is 5 mm.

Movie S5, related to Figure 6.

Locomotion phenotypes of planarians simultaneously depleted from sidewinder genes and DVL1/2.

Speed is accelerated 5 times, bar is 5 mm.

References

Adams, G.M., Wright, R.L., and Jarvik, J.W. (1985). Defective temporal and spatial control of flagellar assembly in a mutant of Chlamydomonas reinhardtii with variable flagellar number. J Cell Biol *100*, 955-964.

Antoniades, I., Stylianou, P., and Skourides, P.A. (2014). Making the connection: ciliary adhesion complexes anchor basal bodies to the actin cytoskeleton. Dev Cell *28*, 70-80.

Azimzadeh, J. (2014). Exploring the evolutionary history of centrosomes. Philos Trans R Soc Lond B Biol Sci *369*.

Azimzadeh, J., Hergert, P., Delouvee, A., Euteneuer, U., Formstecher, E., Khodjakov, A., and Bornens, M. (2009). hPOC5 is a centrin-binding protein required for assembly of full-length centrioles. J Cell Biol *185*, 101-114.

Azimzadeh, J., Wong, M.L., Downhour, D.M., Sanchez Alvarado, A., and Marshall, W.F. (2012). Centrosome loss in the evolution of planarians. Science *335*, 461-463.

Basquin, C., Orfila, A.M., and Azimzadeh, J. (2015). The planarian Schmidtea mediterranea as a model for studying motile cilia and multiciliated cells. Methods Cell Biol *127*, 243-262.

Bengueddach, H., Lemullois, M., Aubusson-Fleury, A., and Koll, F. (2017). Basal body positioning and anchoring in the multiciliated cell Paramecium tetraurelia: roles of OFD1 and VFL3. Cilia *6*, 6.

Boyd, J.S., Gray, M.M., Thompson, M.D., Horst, C.J., and Dieckmann, C.L. (2011). The daughter four-membered microtubule rootlet determines anterior-posterior positioning of the eyespot in Chlamydomonas reinhardtii. Cytoskeleton (Hoboken) *68*, 459-469.

Brown, N.A., and Wolpert, L. (1990). The development of handedness in left/right asymmetry. Development *109*, 1-9.

Bustin, S.A., Benes, V., Garson, J.A., Hellemans, J., Huggett, J., Kubista, M., Mueller, R., Nolan, T., Pfaffl, M.W., Shipley, G.L.*, et al.* (2009). The MIQE guidelines: minimum information for publication of quantitative real-time PCR experiments. Clin Chem *55*, 611-622.

Chen, D., and Zhong, Y. (2015). A computational model of dynein activation patterns that can explain nodal cilia rotation. Biophys J *109*, 35-48.

Clare, D.K., Magescas, J., Piolot, T., Dumoux, M., Vesque, C., Pichard, E., Dang, T., Duvauchelle, B., Poirier, F., and Delacour, D. (2014). Basal foot MTOC organizes pillar MTs required for coordination of beating cilia. Nat Commun *5*, 4888.

Devenport, D. (2014). The cell biology of planar cell polarity. J Cell Biol *207*, 171-179.

Guirao, B., Meunier, A., Mortaud, S., Aguilar, A., Corsi, J.M., Strehl, L., Hirota, Y., Desoeuvre, A., Boutin, C., Han, Y.G.*, et al.* (2010). Coupling between hydrodynamic forces and planar cell polarity orients mammalian motile cilia. Nature cell biology *12*, 341-350.

Gurley, K.A., Rink, J.C., and Sanchez Alvarado, A. (2008). Beta-catenin defines head versus tail identity during planarian regeneration and homeostasis. Science *319*, 323-327.

Hashimoto, M., Shinohara, K., Wang, J., Ikeuchi, S., Yoshiba, S., Meno, C., Nonaka, S., Takada, S., Hatta, K., Wynshaw-Boris, A.*, et al.* (2010). Planar polarization of node cells determines the rotational axis of node cilia. Nat Cell Biol *12*, 170-176.

Hayes, M.J. (2017). Sulphated glycosaminoglycans support an assortment of planarian rhabdite structures. Biol Open *6*, 571-581.

Hoops, H.J., Wright, R.L., Jarvik, J.W., and Witman, G.B. (1984). Flagellar waveform and rotational orientation in a Chlamydomonas mutant lacking normal striated fibers. J Cell Biol *98*, 818-824.

Kunimoto, K., Yamazaki, Y., Nishida, T., Shinohara, K., Ishikawa, H., Hasegawa, T., Okanoue, T., Hamada, H., Noda, T., Tamura, A.*, et al.* (2012). Coordinated Ciliary Beating Requires Odf2-Mediated Polarization of Basal Bodies via Basal Feet. Cell *148*, 189-200.

Kuroda, R., Endo, B., Abe, M., and Shimizu, M. (2009). Chiral blastomere arrangement dictates zygotic left-right asymmetry pathway in snails. Nature *462*, 790-794.

Liu, S.Y., Selck, C., Friedrich, B., Lutz, R., Vila-Farre, M., Dahl, A., Brandl, H., Lakshmanaperumal, N., Henry, I., and Rink, J.C. (2013). Reactivating head regrowth in a regeneration-deficient planarian species. Nature *500*, 81-84.

Marshall, W.F. (2012). Centriole asymmetry determines algal cell geometry. Curr Opin Plant Biol *15*, 632-637.

Matis, M., Russler-Germain, D.A., Hu, Q., Tomlin, C.J., and Axelrod, J.D. (2014). Microtubules provide directional information for core PCP function. Elife *3*, e02893.

Mitchell, B., Jacobs, R., Li, J., Chien, S., and Kintner, C. (2007). A positive feedback mechanism governs the polarity and motion of motile cilia. Nature *447*, 97-101.

Omori, T., Sugai, H., Imai, Y., and Ishikawa, T. (2017). Nodal cilia-driven flow: Development of a computational model of the nodal cilia axoneme. J Biomech *61*, 242-249.

Papon, J.F., Bassinet, L., Cariou-Patron, G., Zerah-Lancner, F., Vojtek, A.M., Blanchon, S., Crestani, B., Amselem, S., Coste, A., Housset, B.*, et al.* (2012). Quantitative analysis of ciliary beating in primary ciliary dyskinesia: a pilot study. Orphanet J Rare Dis *7*, 78.

Park, T.J., Mitchell, B.J., Abitua, P.B., Kintner, C., and Wallingford, J.B. (2008). Dishevelled controls apical docking and planar polarization of basal bodies in ciliated epithelial cells. Nat Genet *40*, 871-879.

Reddien, P.W., Bermange, A.L., Murfitt, K.J., Jennings, J.R., and Sanchez Alvarado, A. (2005). Identification of genes needed for regeneration, stem cell function, and tissue homeostasis by systematic gene perturbation in planaria. Dev Cell *8*, 635-649.

Rink, J.C., Gurley, K.A., Elliott, S.A., and Sanchez Alvarado, A. (2009). Planarian Hh signaling regulates regeneration polarity and links Hh pathway evolution to cilia. Science *326*, 1406-1410.

Robb, S.M., Gotting, K., Ross, E., and Sanchez Alvarado, A. (2015). SmedGD 2.0: The Schmidtea mediterranea genome database. Genesis *53*, 535-546.

Sanchez Alvarado, A., Newmark, P.A., Robb, S.M., and Juste, R. (2002). The Schmidtea mediterranea database as a molecular resource for studying platyhelminthes, stem cells and regeneration. Development *129*, 5659-5665.

Schneider, C.A., Rasband, W.S., and Eliceiri, K.W. (2012). NIH Image to ImageJ: 25 years of image analysis. Nat Methods *9*, 671-675.

Shinohara, K., and Hamada, H. (2017). Cilia in Left-Right Symmetry Breaking. Cold Spring Harb Perspect Biol *9*.

Silflow, C.D., LaVoie, M., Tam, L.W., Tousey, S., Sanders, M., Wu, W., Borodovsky, M., and Lefebvre, P.A. (2001). The Vfl1 Protein in Chlamydomonas localizes in a rotationally asymmetric pattern at the distal ends of the basal bodies. J Cell Biol *153*, 63-74.

Taniguchi, K., Maeda, R., Ando, T., Okumura, T., Nakazawa, N., Hatori, R., Nakamura, M., Hozumi, S., Fujiwara, H., and Matsuno, K. (2011). Chirality in planar cell shape contributes to left-right asymmetric epithelial morphogenesis. Science *333*, 339-341.

Timmons, L., Court, D.L., and Fire, A. (2001). Ingestion of bacterially expressed dsRNAs can produce specific and potent genetic interference in Caenorhabditis elegans. Gene *263*, 103-112.

Vischer, N.O., Verheul, J., Postma, M., van den Berg van Saparoea, B., Galli, E., Natale, P., Gerdes, K., Luirink, J., Vollmer, W., Vicente, M.*, et al.* (2015). Cell age dependent concentration of Escherichia coli divisome proteins analyzed with ImageJ and ObjectJ. Front Microbiol *6*, 586.

Vladar, E.K., Bayly, R.D., Sangoram, A.M., Scott, M.P., and Axelrod, J.D. (2012). Microtubules enable the planar cell polarity of airway cilia. Current biology : CB *22*, 2203-2212.

Vu, H.T., Mansour, S., Kücken, M., Blasse, C., Basquin, C., Azimzadeh, J., Myers, E.W., Brusch, L., and Rink, J.C. (2018). Multi-scale coordination of planar cell polarity in planarians. bioRxiv.

Vu, H.T., Rink, J.C., McKinney, S.A., McClain, M., Lakshmanaperumal, N., Alexander, R., and Sanchez Alvarado, A. (2015). Stem cells and fluid flow drive cyst formation in an invertebrate excretory organ. Elife *4*.

Wan, L.Q., Ronaldson, K., Park, M., Taylor, G., Zhang, Y., Gimble, J.M., and Vunjak-Novakovic, G. (2011). Micropatterned mammalian cells exhibit phenotype-specific left-right asymmetry. Proceedings of the National Academy of Sciences of the United States of America *108*, 12295-12300.

Werner, M.E., Hwang, P., Huisman, F., Taborek, P., Yu, C.C., and Mitchell, B.J. (2011). Actin and microtubules drive differential aspects of planar cell polarity in multiciliated cells. The Journal of cell biology *195*, 19-26.

Wright, R.L., Chojnacki, B., and Jarvik, J.W. (1983). Abnormal basal-body number, location, and orientation in a striated fiber-defective mutant of Chlamydomonas reinhardtii. J Cell Biol *96*, 1697-1707.

Xu, J., Wang, F., Van Keymeulen, A., Rentel, M., and Bourne, H.R. (2005). Neutrophil microtubules suppress polarity and enhance directional migration. Proceedings of the National Academy of Sciences of the United States of America *102*, 6884-6889.

Yubuki, N., and Leander, B.S. (2013). Evolution of microtubule organizing centers across the tree of eukaryotes. Plant J *75*, 230-244.

Zayas, R.M., Cebria, F., Guo, T., Feng, J., and Newmark, P.A. (2010). The use of lectins as markers for differentiated secretory cells in planarians. Dev Dyn *239*, 2888-2897.

Figure 1

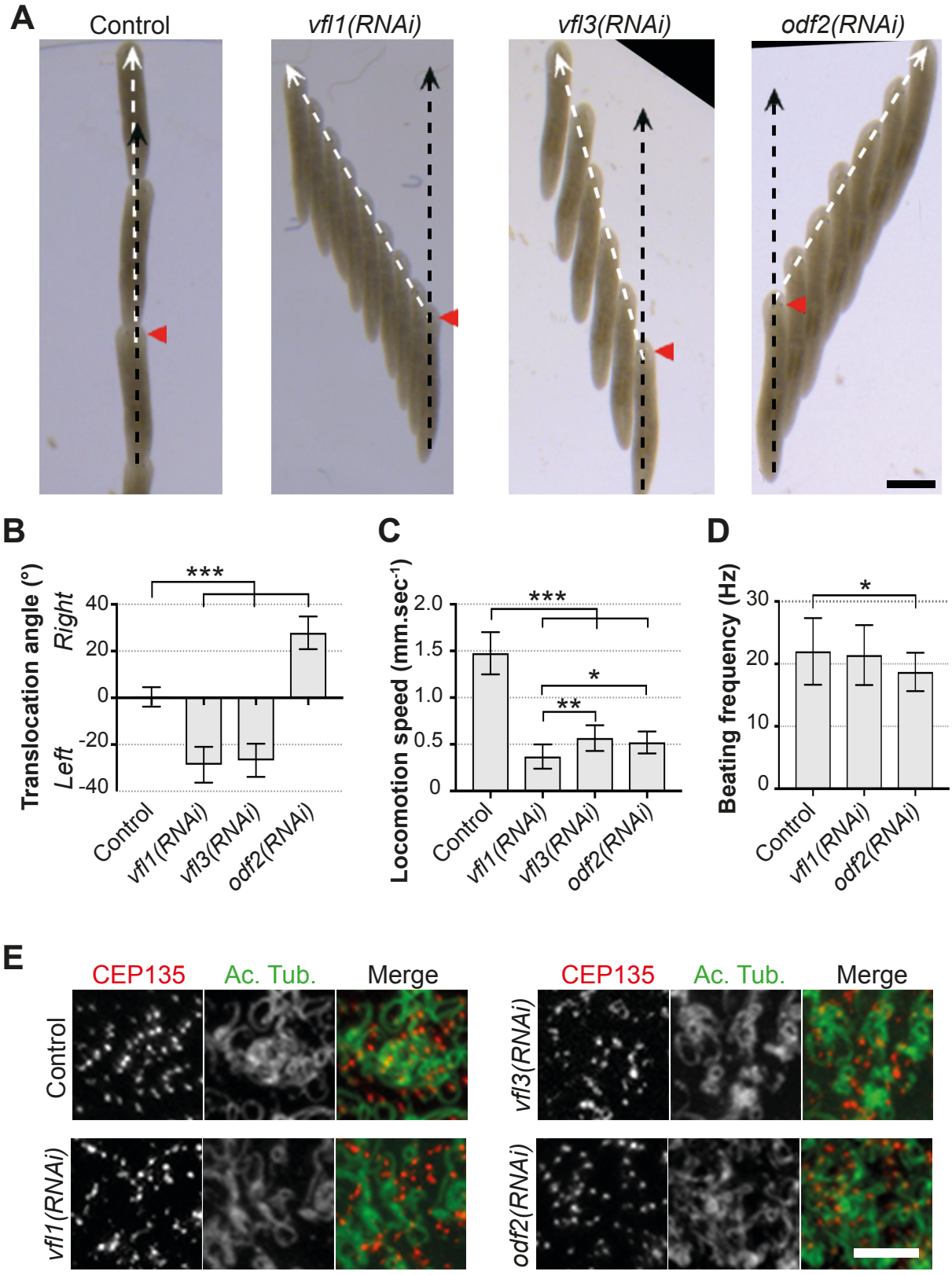
A
Control
vfl1(RNAi)
vfl3(RNAi)
odf2(RNAi)
B
Translocation angle (°)
Right
Left
40
20
0
-20
-40
***
Control
vfl1(RNAi)
vfl3(RNAi)
odf2(RNAi)
C
Locomotion speed (mm.sec-1)
2.0
1.5
1.0
0.5
0
***
*
**
Control
vfl1(RNAi)
vfl3(RNAi)
odf2(RNAi)
D
Beating frequency (Hz)
30
20
10
0
*
Control
vfl1(RNAi)
odf2(RNAi)
E
CEP135
Ac. Tub.
Merge
Control
vfl1(RNAi)
CEP135
Ac. Tub.
Merge
vfl3(RNAi)
odf2(RNAi)

Figure 2

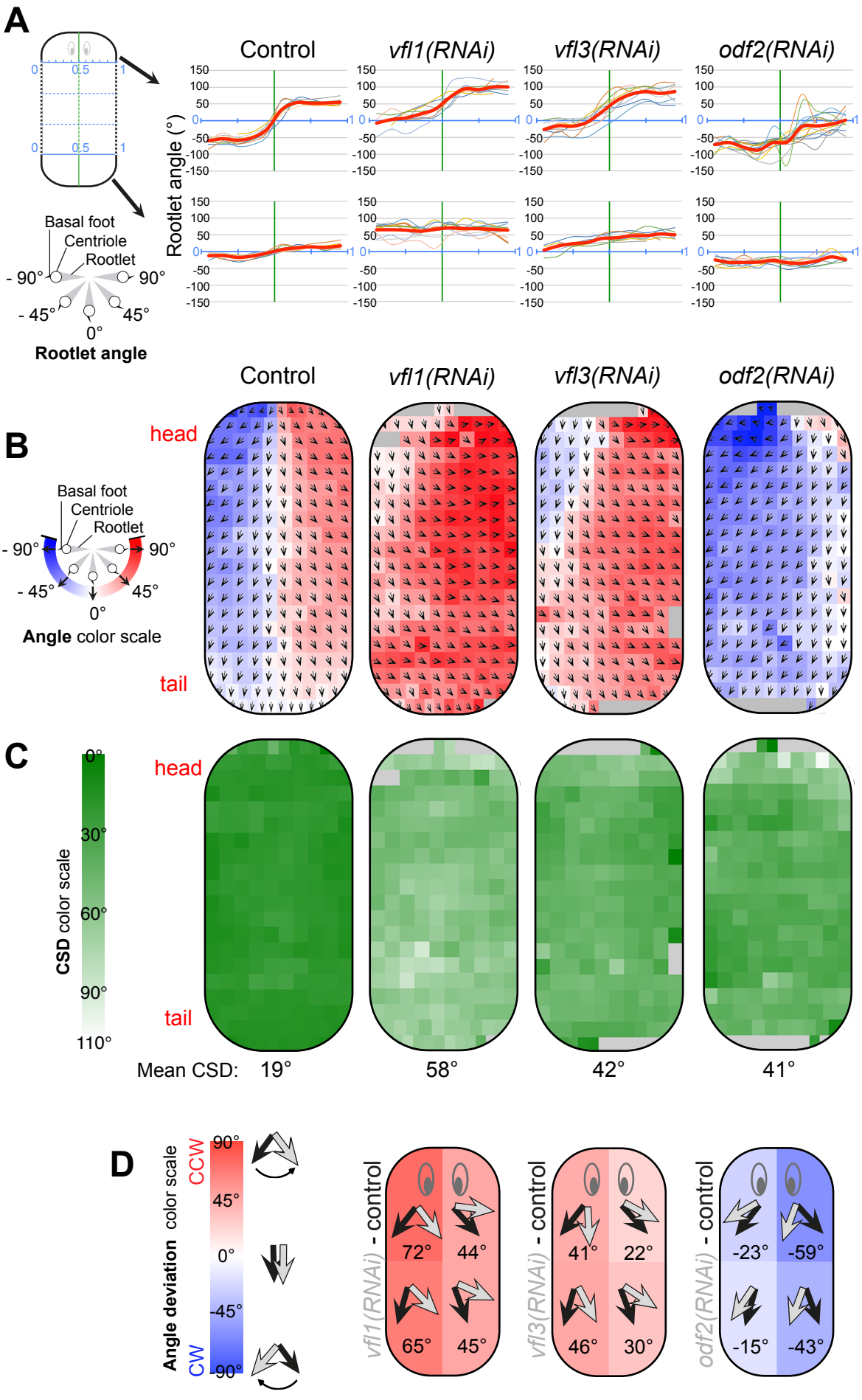
A
Control
vfl1(RNAi)
vfl3(RNAi)
odf2(RNAi)
Rootlet angle (°)
Basal foot
Centriole
Rootlet
- 90°
90°
- 45°
45°
0°
Rootlet angle
B
Control
vfl1(RNAi)
vfl3(RNAi)
odf2(RNAi)
head
tail
Basal foot
Centriole
Rootlet
- 90°
90°
- 45°
45°
0°
Angle color scale
C
CSD color scale
0°
30°
60°
90°
110°
head
tail
Mean CSD: 19° 58° 42° 41°
D
Angle deviation color scale
CCW
CW
90°
45°
0°
-45°
-90°
vfl1(RNAi) - control
72° 44°
65° 45°
vfl3(RNAi) - control
41° 22°
46° 30°
odf2(RNAi) - control
-23° -59°
-15° -43°

Figure 3

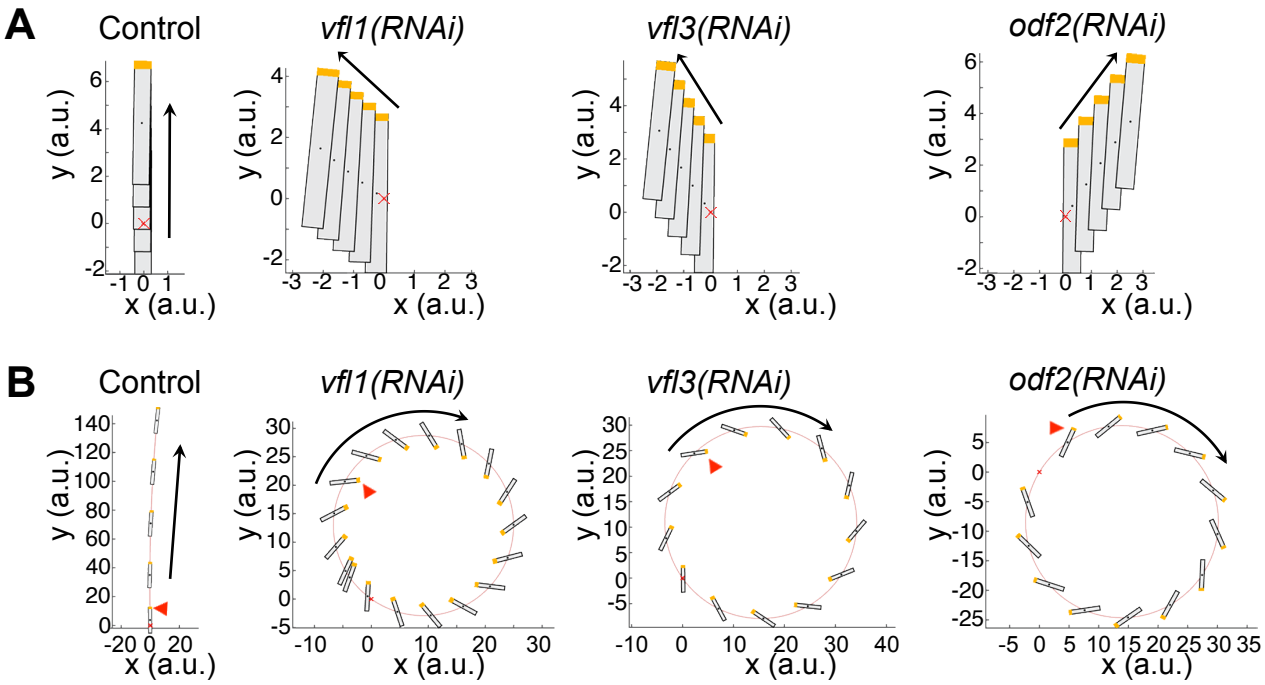
A
Control
vfl1(RNAi)
vfl3(RNAi)
odf2(RNAi)
y (a.u.)
x (a.u.)
B
Control
vfl1(RNAi)
vfl3(RNAi)
odf2(RNAi)
y (a.u.)
x (a.u.)
C
Control
vfl1(RNAi)
vfl3(RNAi)
odf2(RNAi)

Figure 4

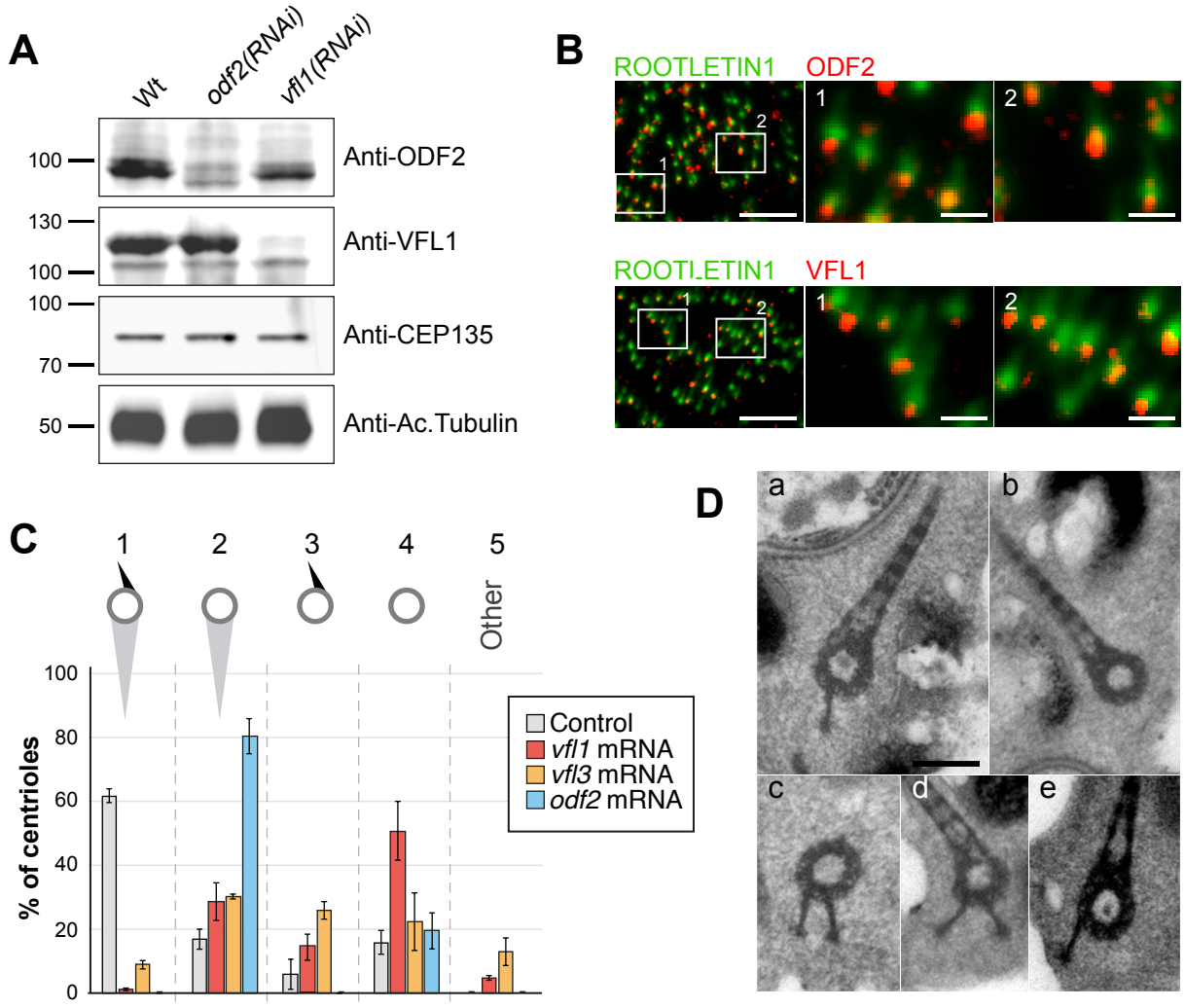
A
Wt
odf2(RNAi)
vfl1(RNAi)
100
Anti-ODF2
130
100
Anti-VFL1
100
70
Anti-CEP135
50
Anti-Ac.Tubulin
B
ROOTLETIN1
ODF2
ROOTLETIN1
VFL1
C
1
2
3
4
5
Other
% of centrioles
100
80
60
40
20
0
Control
vfl1 mRNA
vfl3 mRNA
odf2 mRNA
D
a
b
c
d
e

Figure 5

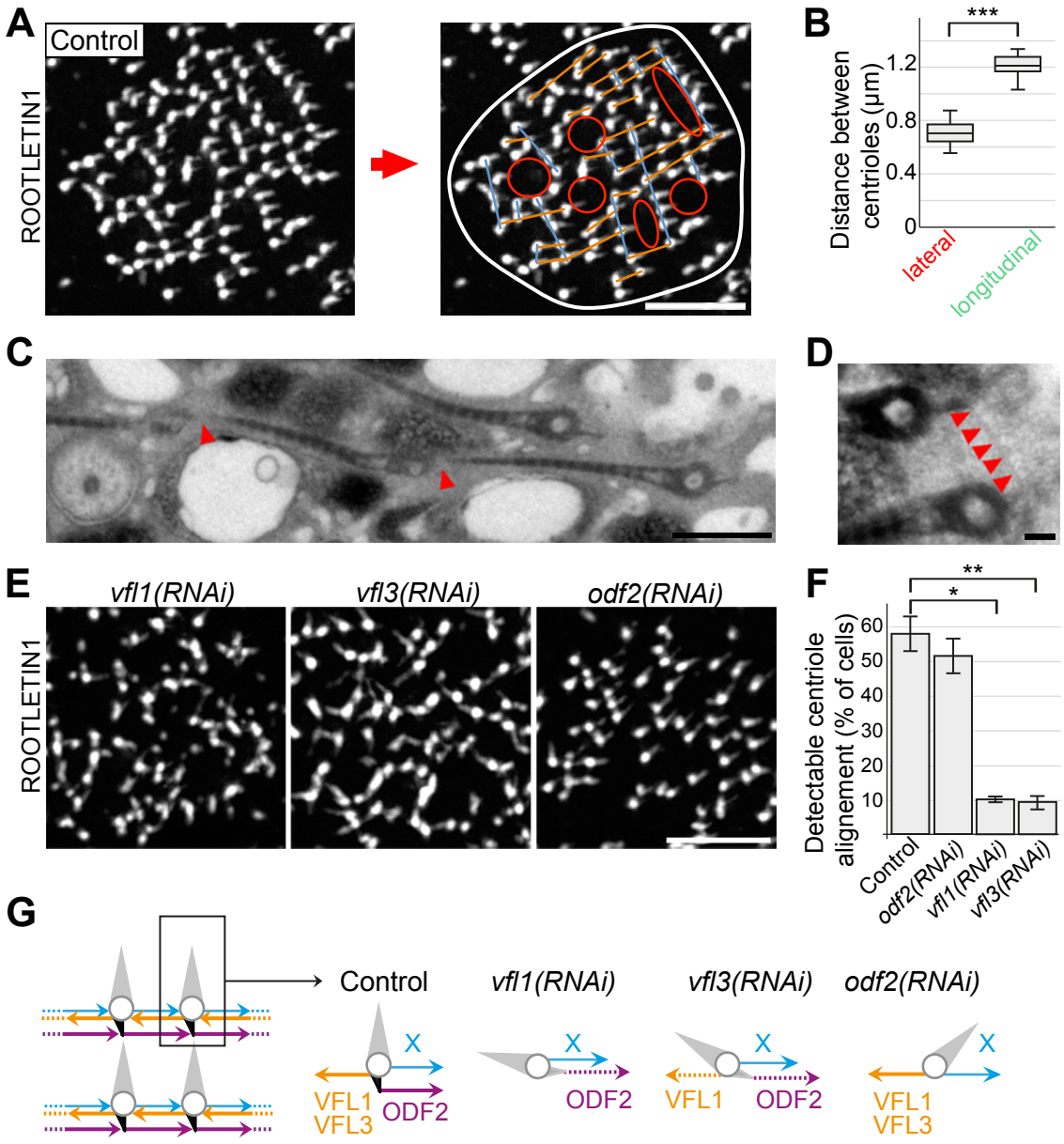
A
Control
ROOTLETIN1
B
***
Distance between centrioles (µm)
1.2
0.8
0.4
0
lateral
longitudinal
C
D
E
vfl1(RNAi)
vfl3(RNAi)
odf2(RNAi)
ROOTLETIN1
F
**
*
Detectable centriole alignement (% of cells)
60
50
40
30
20
10
Control
odf2(RNAi)
vfl1(RNAi)
vfl3(RNAi)
G
Control
vfl1(RNAi)
vfl3(RNAi)
odf2(RNAi)
X
VFL1
VFL3
ODF2

Figure 6

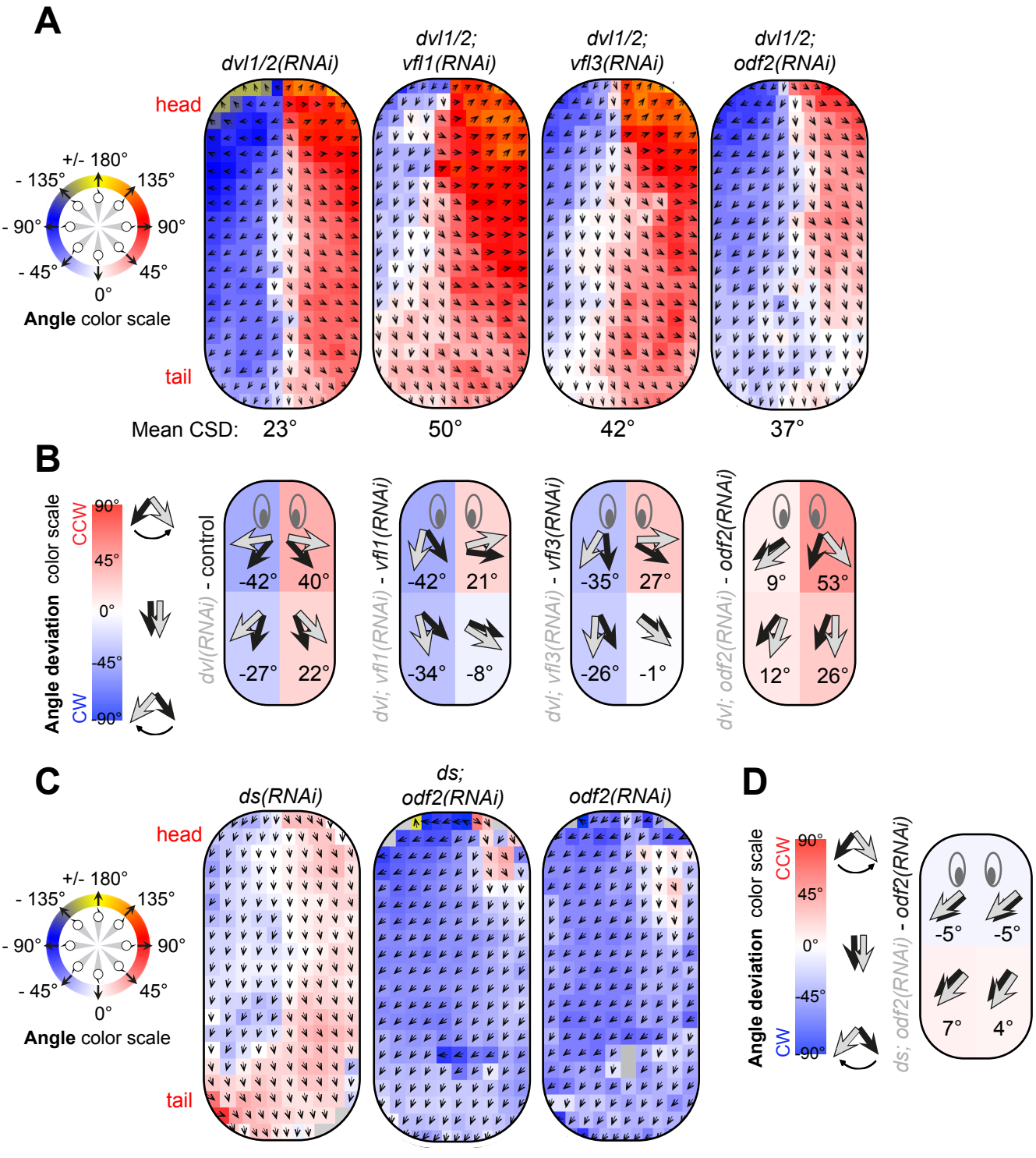
A
dvl1/2(RNAi)
dvl1/2; vfl1(RNAi)
dvl1/2; vfl3(RNAi)
dvl1/2; odf2(RNAi)
head
tail
+/- 180°
- 135°
135°
- 90°
90°
- 45°
45°
0°
Angle color scale
Mean CSD: 23° 50° 42° 37°
B
Angle deviation color scale
CCW
CW
90°
45°
0°
-45°
-90°
dvl(RNAi) - control
-42° 40°
-27° 22°
dvl; vfl1(RNAi) - vfl1(RNAi)
-42° 21°
-34° -8°
dvl; vfl3(RNAi) - vfl3(RNAi)
-35° 27°
-26° -1°
dvl; odf2(RNAi) - odf2(RNAi)
9° 53°
12° 26°
C
ds(RNAi)
ds; odf2(RNAi)
odf2(RNAi)
head
tail
+/- 180°
- 135°
135°
- 90°
90°
- 45°
45°
0°
Angle color scale
D
Angle deviation color scale
CCW
CW
90°
45°
0°
-45°
-90°
ds; odf2(RNAi) - odf2(RNAi)
-5° -5°
7° 4°

Figure 7

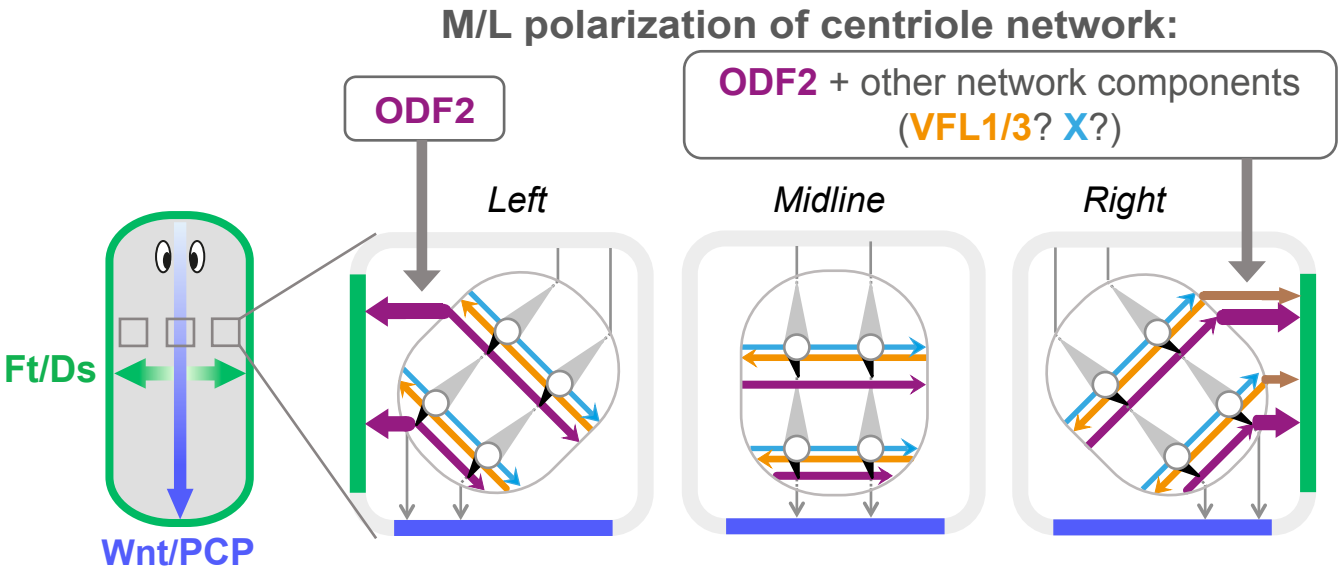
M/L polarization of centriole network:
ODF2
ODF2 + other network components
(VFL1/3? X?)
Left
Midline
Right
Ft/Ds
Wnt/PCP

1. Planarian locomotion relies on a **bilaterally symmetric** array of epidermal cilia

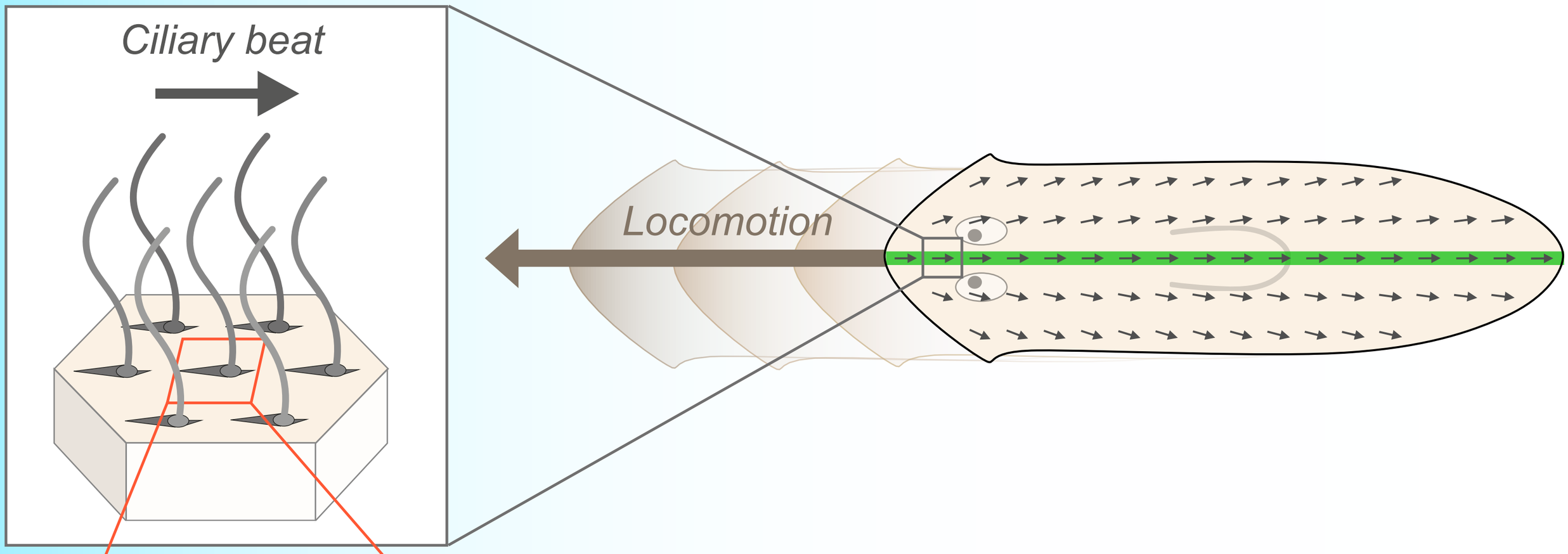

2. The ciliary pattern emerges from a **chiral centriole network** organized via the **balanced action of ODF2 and VFL1/3**